Remote Sensing of Environment 245 (2020) 111842

Contents lists available at ScienceDirect

Remote Sensing of Environment

journal homepage: www.elsevier.com/locate/rse

Estimation of all-sky all-wave daily net radiation at high latitudes from MODIS data

Jiang Chen[a], Tao He[a,*], Bo Jiang[b], Shunlin Liang[c]

[a] School of Remote Sensing and Information Engineering, Wuhan University, Wuhan 430079, China
[b] Faculty of Geographical Science, Beijing Normal University, Beijing 100875, China
[c] Department of Geographical Sciences, University of Maryland, College Park, MD 20742, USA

ARTICLE INFO

Edited by Marie Weiss

Keywords:
Net radiation
High latitudes
Length ratio of daytime
MODIS
High spatial resolution

ABSTRACT

Surface all-wave net radiation (R_n) plays an important role in various land surface processes, such as agricultural, ecological, hydrological, and biogeochemical processes. Recently, remote sensing of R_n at regional and global scales has attracted considerable attention and has achieved significant advances. However, there are many issues in estimating all-sky daily average R_n at high latitudes, such as posing greater uncertainty by surface and atmosphere satellite products at high latitudes, and unavailability of real-time and accurate cloud base height and temperature parameters. In this study, we developed the LRD (length ratio of daytime) classification model using the genetic algorithm-artificial neural network (GA-ANN) to estimate all-sky daily average R_n at high latitudes. With a very high temporal repeating frequency (~6 to 20 times per day) at high latitudes, data from the Moderate Resolution Imaging Spectroradiometer (MODIS) were used to test the proposed method. R_n measurements at 82 sites and top-of-atmosphere (TOA) data of MODIS from 2000 to 2017 were matched for model training and validation. Two models for estimating daily average R_n were developed: model I based on instantaneous daytime MODIS observation and model II based on instantaneous nighttime MODIS observation. Validation results of model I showed an R^2 of 0.85, an RMSE of 23.66 W/m^2, and a bias of 0.27 W/m^2, whereas these values were 0.51, 15.04 W/m^2, and −0.08 W/m^2 for model II, respectively. Overall, the proposed machine learning algorithm with the LRD classification can accurately estimate the all-sky daily average R_n at high latitudes. Mapping of R_n over the high latitudes at 1 km spatial resolution showed a similar spatial distribution to R_n estimates from the Clouds and the Earth's Radiant Energy System (CERES) product. This method has the potential for operational monitoring of spatio-temporal change of R_n at high latitudes with a long-term coverage of MODIS observations.

1. Introduction

All-wave net radiation (R_n), measured at the surface, is a key variable required to estimate surface energy balance (SEB) and surface geophysical processes (Liang et al., 2019; Wild et al., 2013). SEB at the Earth's surface is an important parameter used to characterize land surface processes and interactions and feedback between the land and atmosphere. Thus, it plays a crucial role in agricultural, ecological, hydrological, and biogeochemical processes (Dickinson et al., 2006; Kaminsky and Dubayah, 1997). R_n is the difference between the downward and upward radiation fluxes across the entire shortwave and longwave spectra. R_n is expressed as (Bisht et al., 2005; Liang et al., 2019; Liang et al., 2010b):

$$R_n = R_S^{\downarrow} - R_S^{\uparrow} + R_L^{\downarrow} - R_L^{\uparrow} \quad (1)$$

where are the shortwave downward, shortwave upward, longwave downward, and longwave upward radiation fluxes, respectively.

The absorbed net radiation at natural surfaces should balance outgoing fluxes and can be expressed as (Kato and Yamaguchi, 2005):

$$R_n = G + H + LE \quad (2)$$

where G is the soil heat flux, H is the sensible heat flux, and LE is the latent heat flux. During the daytime, soil heat is conducted into the soil due to lower underground temperature compared to the surface. Stored heat in the soil is released to the atmosphere by longwave radiation overnight. Sensible heat can warm the surface and drive heat exchange from the Earth's surface to the atmosphere. The remaining energy latent heat controls the water cycle process including the transpiration of vegetation and evaporation of land surface water. Specifically, the quantification of R_n and its components have implications for

* Corresponding author.
E-mail address: taohers@whu.edu.cn (T. He).

https://doi.org/10.1016/j.rse.2020.111842
Received 3 December 2019; Received in revised form 21 April 2020; Accepted 21 April 2020

understanding agricultural drought (Wang et al., 2007; Zhao et al., 2013), snow melt (Miller et al., 2018; Van As, 2011; Weston et al., 2007), urban thermal environments (Kato and Yamaguchi, 2005; Kuang et al., 2018; Offerle et al., 2003), and water resource management (Bastiaanssen et al., 2005; Liang et al., 2010a).

R_n can be measured accurately by ground-based instruments; however, only spatially sparse measurements are available at the global scale. Moreover, the necessary instruments (e.g. pyrgeometers) are relatively expensive and require labor for routine maintenance. Satellite remote sensing can continuously and synoptically retrieve R_n with better spatial and temporal coverage as well as reasonable accuracy (Bisht and Bras, 2010; Bisht et al., 2005; Brown and Caldeira, 2017; Huang et al., 2016; Jiang et al., 2018; Jiang et al., 2016; Jung et al., 2019; Wang et al., 2015a). Algorithm development applied to the estimation of R_n at regional and global scales has attracted considerable attention in recent years and achieved significant advances (Amatya et al., 2015; Bisht and Bras, 2010; Jiang et al., 2015; Liang et al., 2019; Mira et al., 2016; Moukomla and Blanken, 2016; Ramírez-Cuesta et al., 2018; Wang et al., 2015a; Zhao et al., 2019; Zhong et al., 2019). The algorithms widely used and validated can be divided into three classes: 1) parameterization algorithms, 2) hybrid algorithms, and 3) empirical algorithms.

Parameterization algorithms estimate R_n using satellite high-level products including atmospheric and surface parameters. For example, Bisht et al. (2005) employed various Moderate Resolution Imaging Spectroradiometer (MODIS) products to estimate the components of R_n under clear-sky conditions and added them together to derive instantaneous R_n. They derived the daytime average R_n using a sinusoidal model to capture the daytime R_n cycle. Bisht and Bras (2010) extended their framework to estimate the daytime average R_n under all-sky conditions over the Southern Great Plains using additional MODIS cloud products, where the accuracy of the model was found to reduce under cloudy-sky conditions. Ryu et al. (2008) assessed the applicability of parameterization algorithms over the heterogeneous and rugged surface and pointed out that the scale mismatch and heterogeneous quality of surface land cover should be carefully considered. Parameterization algorithms have the theoretical foundation and can provide accurate R_n estimates with reliable inputs. For example, the Clouds and the Earth's Radiant Energy System (CERES), which provides useful data to investigate energy budget and global climate change (Brown and Caldeira, 2017), applies a simple and effective parameterization algorithm to produce a Level 2 surface radiation product at the footprint scale of the CERES satellite under both clear- and cloudy- sky conditions (Gupta et al., 2004). Although this Level 2 product has higher spatial resolution, it provides instantaneous R_n estimates instead of daily average R_n. The Level 3 product (CERES-SYN) provides daily average R_n with an aggregated 1° spatial resolution. Its R_n data are estimated using Fu-Liou's radiative transfer model with the atmospheric and surface parameters used as model inputs (Fu and Liou, 1993; Wielicki et al., 1996).

Hybrid algorithms generally include two steps: 1) a large set of top-of-atmosphere (TOA) observations and corresponding surface R_n datasets, representing different surface and atmosphere conditions, is simulated by a radiative transfer model, and 2) empirical relationships between TOA reflectance or radiance and R_n are built by applying simple statistical methods or machine learning (Wang et al., 2015a; Wang et al., 2012). Hybrid algorithms can also be used to estimate R_n under clear-sky conditions; however, this algorithm has limited application under cloudy-sky conditions because real-time cloud base height and temperature are important variables in quantifying longwave radiation components (Wang et al., 2018; Zhou and Cess, 2001). Furthermore, Wang et al. (2015a) found that R_n estimates as the complete parameter had performed better than separating shortwave and longwave radiation parts. The main difficulty in estimating R_n is that the estimation of longwave radiation components under cloudy-sky conditions remains a challenge due to the unavailability of atmospheric parameters below a cloud layer (Duarte et al., 2006; Wang et al., 2018; Zhou et al., 2007).

R_n has been demonstrated to be significantly related to shortwave radiation fluxes, except for polar regions (Alados et al., 2003; Guo and Cheng, 2018; Hu et al., 2011; Zhou et al., 2013). Empirical algorithms indirectly estimate R_n using the relationship between R_n, shortwave radiation fluxes, and other auxiliary data (Alados et al., 2003; Huang et al., 2016; Jiang et al., 2015; Zhou et al., 2013). Utilizing this theoretical foundation, some daytime average R_n products have been developed over land surfaces and present good overall accuracy (Jiang et al., 2018; Jiang et al., 2016). This method was further extended to derive daily average R_n (the sum of daytime and nighttime values), but was found to have dissatisfactory accuracy at high latitudes (Babar et al., 2019; Raschke et al., 2006). This is because shorter daytime duration and polar night phenomena result in unstable R_n estimates if one only leverages shortwave radiation to estimate R_n at high latitudes.

High latitudes are typically more sensitive to climate change related to global warming (Brown and Caldeira, 2017; Niu et al., 2010; Van Den Broeke et al., 2004). In recent decades, the polar ice sheets such those as in Greenland, Alaska, and the Antarctic Peninsula land ice have undergone massive melting events, playing a crucial role in regional climate change and global sea level rise (Box et al., 2018; He et al., 2013; Van As, 2011; Vaughan and Doake, 1996). Changes in R_n are one of the driving forces that determine ice sheet mass balance. Some researchers have used a limited number of radiation observation sites to study radiation budget at high latitudes; however, the spatial and temporal variation of R_n has not yet been fully understood (Kuipers Munneke et al., 2018; Miller et al., 2018; Van As, 2011; van den Broeke et al., 2008). Existing satellite products, such as CERES data, provide daily R_n with 1° spatial resolution, which is insufficient for radiation budget analysis over ice sheets, particularly for ablation zones. Jia et al. (2016) undertook a comprehensive evaluation of the accuracy of the CERES-SYN product using globally distributed ground-based measurements. They concluded that the R_n estimates from the CERES-SYN product are accurate at a global scale, this accuracy, however, is relatively lower at high latitudes. As regards other products such as the Global Energy and Water Experiment (GEWEX), International Satellite Cloud Climatology Project (ISCCP), and the Cloud, Albedo and Radiation dataset (CLARA), CERES products are superior to them in terms of general accuracy (Gui et al., 2010; Jia et al., 2018).

To date, very few efforts have been made to remotely estimate shortwave radiation fluxes at high latitudes (Babar et al., 2019; Babar et al., 2020), and fewer works focus especially on R_n (Babar et al., 2019; Gui et al., 2010; Niu et al., 2010). Of the remote sensing algorithms mentioned above, parameterization algorithms are not applicable due to posing greater uncertainty by surface and atmosphere satellite products at high latitudes (Gusain et al., 2019; Hall et al., 2018). Hybrid algorithms have limited capability for estimating R_n under cloudy-sky conditions due to the unavailability of real-time and accurate cloud base height and temperature variables (Wang et al., 2018; Zhou and Cess, 2001). In addition, large solar zenith angle (SZA) usually occurs at high latitudes. Hybrid algorithms have larger errors when SZA is large owing to the inherent limitations of radiative transfer simulation at large SZA (Wang et al., 2015a). The existing algorithms with the help of shortwave radiation fluxes have unacceptable performance with low accuracy or retrieval failure at high latitudes (Jia et al., 2018; Raschke et al., 2006; Wang et al., 2015a). In contrast, machine learning algorithms do not need real-time and accurate surface and atmosphere parameters; however, they have comparable performance. This method of estimating radiation fluxes is becoming increasingly popular using collected in situ radiation data and matched satellite observations (Deo et al., 2019; Ghimire et al., 2018; Peng et al., 2019; Wei et al., 2019; Ying et al., 2019; Zhou et al., 2018). Recently, Jung et al. (2019) also estimated daily net radiation with machine learning algorithms at 0.0833-degree resolution using MODIS and at 0.5-degree resolution using remote sensing and meteorological data. Therefore, the issues in

R_n estimates at high latitudes motivate us to explore the availability of machine learning algorithms to derive daily average R_n.

The MODIS is a key sensor on board the Terra and Aqua satellites, scanning the land surface about 6–20 times daily at high latitudes. Multiple overpasses during a day are critical for modeling diurnal changes in R_n, with good potential to improve the accuracy of daily average R_n estimates (Wang et al., 2015b). MODIS has a unique advantage on this issue compared to other sensors. For example, geostationary satellites do not perform suitable observations at high latitudes due to large viewing angles, limiting their use. The main objective of this study is to develop an operational scheme for estimating all-sky daily average R_n with 1 km spatial resolution from MODIS data at high latitudes. This paper is organized as follows: the data and methods for the R_n estimation are described in Section 2, and the results are presented and discussed in Section 3. Finally, a conclusion is provided in Section 4.

2. Data and method

Two kinds of satellite data were employed in this study; MODIS data and CERES-SYN data. The former was used to estimate the daily average R_n at high latitudes, while the latter was selected to compare the daily average R_n estimates from MODIS data using the proposed algorithm. Ground measurements from global observation networks were also collected to train and validate the daily average R_n estimates. A machine learning algorithm was applied to build the specific retrieval model, and a classification model scheme constrained by the length ratio of daytime (LRD) was employed to develop the LRD classification model.

2.1. MODIS products

Collection 6 MODIS TOA observation data (MOD021KM and MYD021KM) and corresponding geolocation data (MOD03 and MYD03) from 2000 to 2017 were collected with the MODIS Level-1B dataset. MOD021KM and MYD021KM, the Calibrated Earth View dataset with l km resolution, were used to derive TOA reflectance at shortwave bands and TOA radiance at longwave bands (Toller et al., 2009). MOD03 and MYD03 products with l km resolution were utilized to match pairs between in situ observed R_n data and satellite TOA observations. They also provided the SZA, solar azimuth angle (SAA), viewing zenith angle (VZA), viewing azimuth angle (VAA), and surface elevation variables. MODIS has 36 bands including 20 visible and shortwave infrared (VSWIR) bands as well as 16 thermal infrared bands. Shortwave bands 8–16 are typically not used in land remote sensing as they are designed for aquatic environment applications, distinguished by the low threshold of saturation (Wang et al., 2015a). In this study, considering different band combinations as independent variables to test model performance, TOA reflectance of eight shortwave bands (B1-B7 and B19) were selected to explain the contributions of shortwave radiation fluxes to R_n. The water vapor absorption band, B19, was used to account for the water vapor effect on shortwave net radiation (Wang et al., 2015a, 2015b; Zhang et al., 2019). The TOA radiance of 10 longwave bands (B27-B36) were used to explain the contributions of longwave radiation fluxes to R_n that are consistent with previous studies (Cheng and Liang, 2016; Wang et al., 2015a; Wang et al., 2012; Wang and Liang, 2009; Wang et al., 2009; Zhou et al., 2018). The wavelengths of the shortwave and longwave bands used in this study are shown in Table 1.

2.2. CERES-SYN product

The CERES-SYN product has been demonstrated to be accurate at the global scale and was employed to study the spatio-temporal change of R_n (Brown and Caldeira, 2017; Jia et al., 2016). R_n estimates from the CERES-SYN product are highly accurate for the mid and low latitudes; however, its accuracy is lower for high latitudes (Jia et al., 2016; Jia et al., 2018). The CERES-SYN Edition4 product including hourly $R_S^{\downarrow}$, $R_S^{\uparrow}$, $R_L^{\downarrow}$, $R_L^{\uparrow}$ parameters under all-sky conditions at 1° spatial resolution was used to derive daily average R_n. A previous study evaluated the accuracy of CERES-SYN at high latitudes (Jia et al., 2016), the validation results have an RMSE of more than 33.56 W/m^2 and a bias of more than 3.43 W/m^2. The low accuracy of the CERES-SYN at high latitudes may be attributed to its coarse spatial resolution of 1° that cannot capture land cover complexity, and the large errors in snow cover areas (Jia et al., 2016). Although CERES-SYN shows relatively lower accuracy at high latitudes (Jia et al., 2018), it is still an available reference product to compare overall spatial pattern with MODIS-derived R_n estimates.

2.3. Ground measurements

Over the past several decades, globally distributed ground-based radiation flux observation networks have provided continuous in situ R_n measurements widely used in scientific research. We collected in situ R_n measurements from 2000 to 2017 at high latitudes where the latitude was greater than 60°. R_n data at 82 sites from eight observation networks were used for model training and validation. These included 19 sites from the European Fluxes Database Cluster (EFDC), 9 sites from FLUXNET, 17 sites from AmeriFlux, 3 sites from the Baseline Surface Radiation Network (BSRN), 2 sites from the Coordinated Energy and Water Cycle Observations Project (CEOP), 25 sites from the Programme for Monitoring of the Greenland Ice Sheet (PROMICE), 4 sites from the Institute for Marine and Atmospheric Research (IMAU), and 3 sites from AsiaFlux. Fig. 1 shows the spatial distribution of the 82 in situ observation sites used in this study.

The EFDC was built to set up flux measurement infrastructure to provide high quality and standard field observed data from different ecosystems to the atmosphere. To routinely observe carbon dioxide and water vapor exchange, regional networks in North, Central, and South America as well as Europe, Asia, Africa, and Australia are connected to constitute FLUXNET, the global observation network. The FLUXNET network, distributed across most of the world's climate zones and representative biomes, contains more than 800 active and historic flux observation sites. The AmeriFlux network, supported and maintained by the Lawrence Berkeley National Laboratory (LBNL), began collecting data in 1996 and grew from approximately 15 sites in 1997 to over 110 current active sites. The BSRN network is a project of the GEWEX supported by the World Climate Research Programme (WCRP). The BSRN aims to understand climate change resulting from significant changes in SEB at the Earth's surface. The CEOP network has established globally dispersed sites to monitor and predict water resources at the local or continental scales. The regional network PROMICE, includes 25 fully automatic stations in Greenland, and is organized to measure ice melt, climate, and ice movement and monitor the mass loss over Greenland. The IMAU at Utrecht University has set up several automatic weather stations (AWS) on glaciers in different locations around the world such as Greenland, the Alps, Norway, Iceland, and Svalbard. The mission of IMAU is to improve our understanding of the exchange processes between ice/snow surface and atmosphere as well as the dynamic changes of glaciers and ice sheets. AsiaFlux is a regional observation network bringing researchers in Asia together to study the variation of carbon dioxide, water vapor, and energy exchanges between terrestrial ecosystems and the atmosphere across various time scales.

Note that there are some overlapping or nearby sites between networks. To avoid data repetition and confusion, we selected one set of data for each site. Strict data quality control should be carefully conducted prior to the aggregation of in situ R_n data to daily 24-h average values (Jiang et al., 2015). The quality control of R_n data was performed on a site-by-site basis using three steps: 1) removing raw data records labeled with a bad quality flag, 2) checking the temporal

Table 1
The wavelengths of the shortwave and longwave bands used in this study.

Shortwave bands			Longwave bands		
Band No.	Bandwidth (μm)	Center Wavelength (μm)	Band No.	Bandwidth (μm)	Center Wavelength (μm)
B1	0.620–0.670	0.645	B27	6.535–6.895	6.715
B2	0.841–0.876	0.858	B28	7.175–7.475	7.325
B3	0.459–0.479	0.469	B29	8.400–8.700	8.550
B4	0.545–0.565	0.555	B30	9.580–9.880	9.730
B5	1.230–1.250	1.240	B31	10.780–11.280	11.030
B6	1.628–1.652	1.640	B32	11.770–12.270	12.020
B7	2.105–2.155	2.130	B33	13.185–13.485	13.335
B19	0.915–0.965	0.940	B34	13.485–13.785	13.635
			B35	13.785–14.085	13.935
			B36	14.085–14.385	14.235

continuity, and 3) manually inspecting and removing unreasonable values. The daily average R_n values were calculated when at least one valid observation was available for each hour during a 24-h cycle.

2.4. Genetic algorithm-artificial neural network

2.4.1. Artificial neural network

An artificial neural network (ANN) is composed of interconnections between the input, hidden, and output layers. Its key features include network topology, neuron characteristics, and training or learning rules (Lippmann, 1987; Peng et al., 2019). The type of single hidden layer ANN trained by a feed-forward back-propagation algorithm (FFBPA) is a frequently used scheme for regression and forecasting (Ghimire et al., 2018; Khajeh et al., 2012), where various inputs and an output are completely connected with one hidden layer. The superiority of the FFBPA as reflected by its lack of complexity, has similar nonlinear prediction capabilities compared with other approaches (Han et al., 2007). By minimizing the mean square error between the ANN output and actual observed data, a reliable ANN is generated using a training process to adjust the weight concerned with the transfer functions between neurons. The major challenge in building a back propagation ANN is weight optimization, which highly influences the performance of the ANN (Kayarvizhy et al., 2013). The back propagation ANN will easily get trapped in a local minimum value, which may result in a failure to obtain a global optimal solution (Ghimire et al., 2018). The estimation of R_n by the ANN was calculated as:

$$Y = f(wX + b) \tag{3}$$

where Y is the estimated R_n, f is the transfer function of the hidden layer, w is the weight, X is the input vector, and b is the neuron bias.

2.4.2. Genetic algorithm

Genetic algorithm (GA) is a global optimization method inspired by natural selection and species population evolution mechanisms (Holland, 1975). The basic notion of GA is that every chromosome, corresponding to a solution of the optimization issue, determines the degree of excellence of each generation by the predefined fitness function. A GA is specified by five components: encoding, population initialization, individual selection, crossover, and mutation. The GA processing involved five steps: (1) input variables encoded in binary (zeros and ones) were regarded as chromosomes; (2) the GA needs a set of possible initial solutions to begin operating, and all input chromosomes (population) were first selected; (3) a predefined fitness function was employed to assess whether the fitness of every chromosome met the constraint; (4) if it is met, the output was selected as the result, otherwise chromosomes with better fitness remained to generate offspring from reproduction, crossover, and mutation; (5) the fitness of every new chromosome was assessed again. The last step was repeated until the fitness met the predefined constraint.

2.4.3. Optimized ANN based on GA

Two parameters (w, weight; b, bias), were key factors directly determining the ANN prediction model accuracy. Determining the best w and b is an issue for ANN model optimization that needs to be addressed. GA, a typical optimization algorithm, was employed for w and b optimization, where w and b values were equal to the best chromosome. After deriving the optimal parameters, the GA-ANN model was used to estimate R_n. The main steps of GA-ANN for estimating R_n were:

(1) Splitting the dataset: the dataset was randomly divided into two classes; 70% to train the model and 30% for model validation. All input and output variables were normalized to the same scaling values ranging from 0 to 1.
(2) Setting the parameters of ANN: there was no clear mathematical equation to determine the optimal number of neurons in a hidden layer of the ANN model; thus, the number of neurons was determined through trial and error (Ghimire et al., 2018; Khajeh et al., 2012), which was feasible and generally accepted. Neurons ranging from 5 to 50, in increments of 5, were tested. Furthermore, the Levenberg–Marquardt back propagation (LM), a very well suited and generally accepted method, was employed to train the ANN model (Khajeh et al., 2012; Saini and Soni, 2002).
(3) Setting the GA parameters: the crossover probability, mutation probability, and number of iterations were set to 0.9, 0.3, and 10,

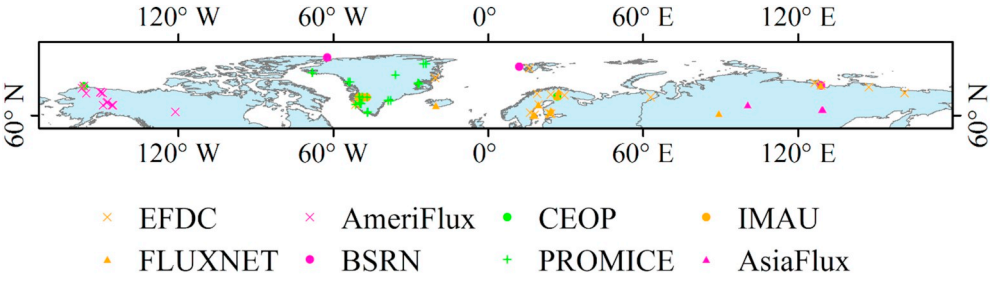

Fig. 1. Spatial distribution of 82 in situ sites from eight radiation fluxes networks.

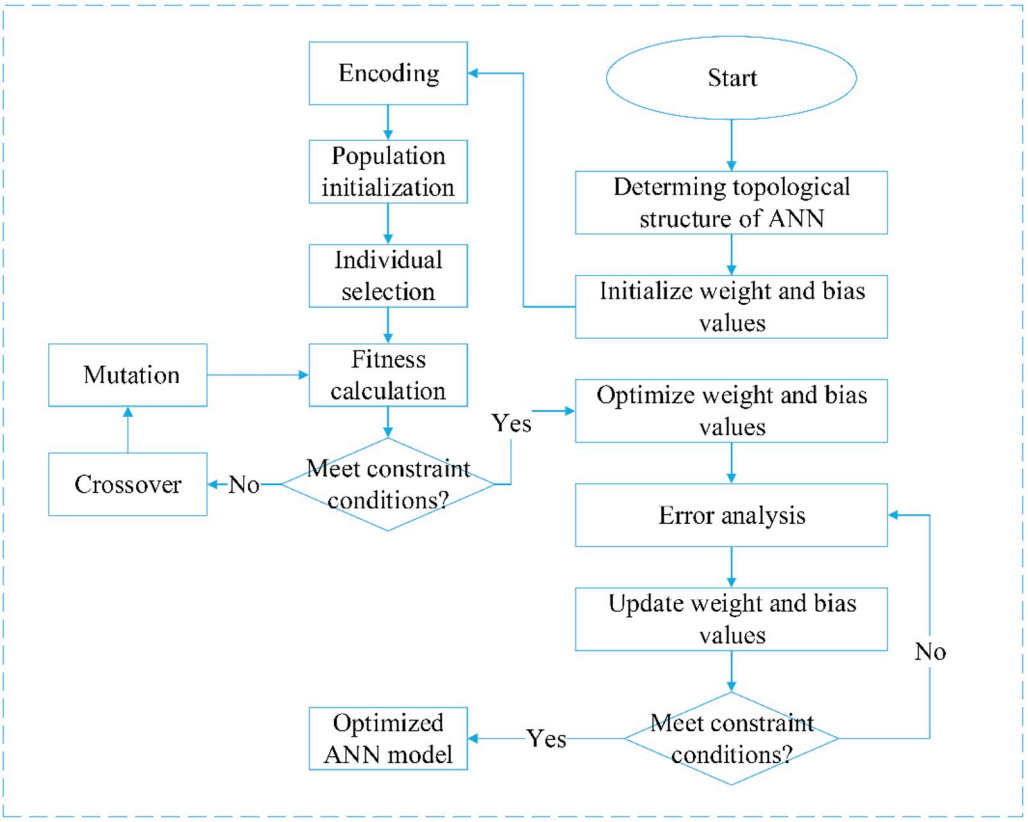

Fig. 2. Flowchart for constructing the GA-ANN model.

respectively. No theoretical approach could be applied to accurately derive optimal population size. During practical operation, an optimal population size of 100 was chosen based on the sensitivity test with the defined crossover and mutation probability.

(4) Optimizing parameters *w* and *b* of ANN using the GA: individual selection, crossover, and mutation were conducted within the genetic algorithm to find the optimal *w* and *b* values.

The parameters *w* and *b* were optimized by the GA. Calculating the mean square error between the ANN output and in situ measured daily average R_n, error analysis was conducted. Then, current *w* and *b* were updated by the optimized values. The ANN model was developed to estimate R_n using these optimal *w* and *b* parameters. The flowchart of constructing the GA-ANN model is shown in Fig. 2.

2.5. Model development

The ground measurements of the daily average R_n for 82 sites at high latitudes from 2000 to 2017 were treated as output of the GA-ANN model. Remote sensing data derived from MODIS were used as input variables of the GA-ANN model, including the TOA reflectance of eight shortwave bands (B1-B7 and B19), TOA radiance of 10 longwave bands (B27-B36), SZA, VZA, relative azimuth angle (RAA), and elevation. Shortwave bands were used to explain the contributions of shortwave radiation fluxes to R_n (Wang et al., 2015a; Wang et al., 2012; Wei et al., 2019; Ying et al., 2019; Zhang et al., 2019), and longwave bands were used to explain the contributions of longwave radiation fluxes to R_n (Cheng and Liang, 2016; Cheng et al., 2017; Wang et al., 2018; Wang and Liang, 2009; Wang et al., 2009; Zhou et al., 2018). Controlling the atmospheric mass, surface elevation was found to have an impact on surface radiation budget (He et al., 2015). To address this, the elevation may act as the model regression variable (Wang and Liang, 2009; Zhou et al., 2018; Zhou et al., 2019). The LRD is defined as the proportion of the total daytime duration to the entire day. The LRD significantly changes with time and space at high latitudes, especially in the polar regions. The LRD ranges from 0 to 1 and if the LRD is greater than a threshold value, daily average R_n has a significant relationship with daytime average R_n. Many studies have used this rule to estimate R_n (Alados et al., 2003; Guo and Cheng, 2018; Huang et al., 2016; Jiang et al., 2015; Zhou et al., 2013). However, only using this method is problematic as at times there are short daytime days at high latitudes. If LRD is less than a threshold value, daily average R_n is primarily determined by the nighttime average R_n. It is an interesting finding, and can be used to supplement the solution of estimating daily average R_n for short daytime days. Besides, when the length of daytime is short at high latitudes, there may be no MODIS observations in the daytime. Correspondingly, when the length of nighttime is short at high latitudes, there may be no MODIS observations in the nighttime. By using an LRD threshold value, we attempted to develop the LRD classification model for estimating daily average R_n. To build our LRD classification model, the relationships between daytime average, nighttime average, and daily average R_n were explored based on ground measurements at high latitudes. Ground measured R_n values were first integrated to derive the daytime average, nighttime average, and daily average R_n. Using the LRD values ranging from 0 to 1 in increments of 0.05, the R_n dataset was classified into 20 groups. For the 20 group's data, linear models were developed between daytime average, nighttime average, and daily average R_n to explore the different contributions of daytime/nighttime average R_n to daily average R_n. Moreover, different LRD values were used to build the LRD classification model to determine the optimal LRD threshold value.

The MODIS cloud product poses great uncertainty at high latitudes because of issues in distinguishing between cloud, snow, or ice. Ying et al. (2019) demonstrated that machine learning is a practical algorithm to estimate radiation fluxes under all-sky conditions using a single model. Therefore, sky conditions were not distinguished in the

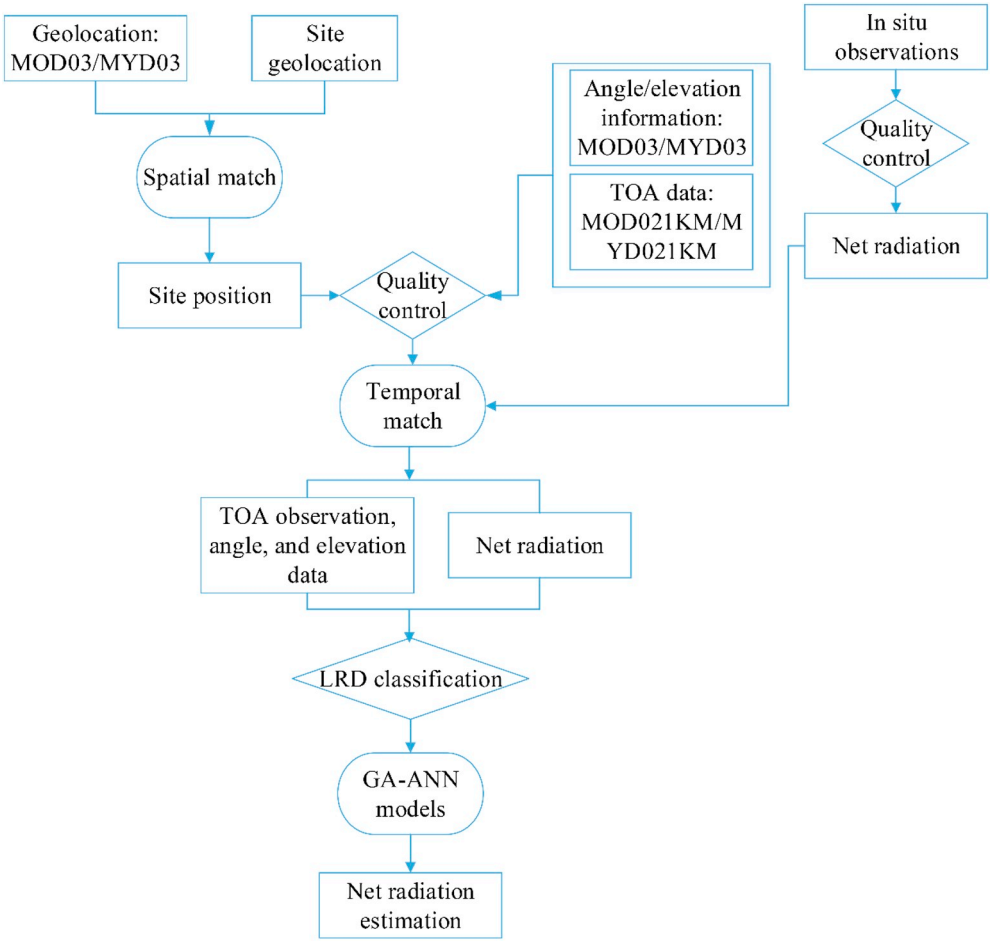

Fig. 3. Flowchart of the study scheme for estimating daily average R_n.

GA-ANN model. Furthermore, instantaneous MODIS observations were used to estimate daily average R_n as there was a relationship between instantaneous and daily average R_n (Bisht and Bras, 2010; Huang et al., 2016; Wang et al., 2015b; Wang et al., 2010; Zhang et al., 2019). Employing both Terra MODIS and Aqua MODIS data, we derived daily average R_n estimates at 1 km spatial resolution based on the LRD classification model developed using the GA-ANN algorithm. The flowchart of the study scheme used to estimate R_n is shown in Fig. 3. There is usually more than one MODIS observation at high latitudes due to its orbit design. In these cases, we derived multiple daily average R_n estimates in one day and all estimates for that day were averaged to obtain the final daily average R_n.

3. Results and discussion

3.1. Relationship between daytime average R_n, nighttime average R_n, and daily average R_n

Table 2 lists the statistical indicators of the linear model developed between the daytime average, nighttime average, and daily average R_n values for the 20 group's data. The R^2 and RMSE values changed with the LRD values, indicating that average R_n during daytime and nighttime had different contribution to the daily average R_n when the LRD varied. The linear model between the daytime average R_n and daily average R_n had increased R^2 (0.030–0.999) and decreased RMSE (21.39–1.04 W/m^2) with the increase of the LRD. In general, the daytime average R_n became increasingly important in estimating the daily average R_n under higher LRD values. The nighttime average R_n equals longwave net radiation, as there is an absence of shortwave radiation at

Table 2
Statistical indicators of linear models developed between daytime average R_n, nighttime average R_n, and daily average R_n under different LRD values.

Min LRD	Max LRD	Model performance between daytime average R_n and daily average R_n		Model performance between nighttime average R_n and daily average R_n	
		R^2	RMSE (W/m^2)	R^2	RMSE(W/m^2)
0.00	0.05	0.030	21.39	0.999	0.20
0.05	0.10	0.675	13.30	0.997	1.28
0.10	0.15	0.784	9.91	0.994	1.68
0.15	0.20	0.776	10.86	0.987	2.63
0.20	0.25	0.737	11.19	0.973	3.61
0.25	0.30	0.718	11.75	0.924	6.10
0.30	0.35	0.718	12.45	0.841	9.36
0.35	0.40	0.713	11.94	0.738	11.42
0.40	0.45	0.696	12.70	0.414	17.64
0.45	0.50	0.782	11.42	0.474	17.75
0.50	0.55	0.892	11.09	0.164	30.81
0.55	0.60	0.959	9.59	0.050	46.32
0.60	0.65	0.972	8.57	0.034	50.63
0.65	0.70	0.981	8.06	0.031	57.47
0.70	0.75	0.989	6.86	0.009	63.85
0.75	0.80	0.991	6.09	0.001	65.27
0.80	0.85	0.997	3.74	0.026	68.90
0.85	0.90	0.996	3.15	0.004	49.48
0.90	0.95	0.998	2.03	0.038	49.49
0.95	1.00	0.999	1.04	0.014	54.53

night. With a decrease in the LRD, the linear model between the nighttime average R_n and daily average R_n had increased R^2 (0.014–0.999) and decreased RMSE (54.53–0.20 W/m^2), showing that the nighttime average R_n played a significant role in estimating the daily average R_n under relatively lower LRD values. An adjacent group with similar LRD exhibited a similar phenomenon. For example, in two groups, where the LRD ranged from 0.15 to 0.20 and 0.20 to 0.25, daily average R_n demonstrated a better relationship with the nighttime average R_n than with the daytime average R_n; the R^2 (0.987 and 0.973) were very close. Therefore, using an LRD threshold, it is possible to develop the LRD classification model to estimate the daily average R_n. Furthermore, instantaneous MODIS observation was used directly to estimate the daily average R_n due to the relationship between the instantaneous R_n and daily average R_n (Bisht and Bras, 2010; Huang et al., 2016; Wang et al., 2015b; Wang et al., 2010; Zhang et al., 2019). The operability and acceptable accuracy of this scheme have been previously proven (Wang et al., 2015b; Zhang et al., 2019). In light of these findings, daily average R_n was estimated from instantaneous daytime MODIS observations when the daytime duration was relatively long. Conversely, the daily average R_n was estimated from instantaneous nighttime MODIS observations when the nighttime duration was relatively long.

3.2. LRD classification threshold

To study and determine the LRD threshold applied to develop the LRD classification model, a dataset including the daytime average, nighttime average, and daily average R_n was divided into two groups based on different LRD values. One group, where LRD was greater than the classification threshold, was used to investigate the relationship between the daytime average R_n and daily average R_n (expressed as relationship I). The other group where LRD was less than the classification threshold was used to explore the relationship between the nighttime average R_n and daily average R_n (expressed as relationship II). Table 2 shows that 1) when the LRD ranges from 0 to 0.3, relationship II had higher R^2 values (0.999–0.924) than relationship I (0.030–0.718); 2) however, for the LRD ranging from 0.45 to 1.0, relationship I had higher R^2 values (0.782–0.999) than relationship II (0.474–0.014). According to Figs. 4, 0.30 and 0.45 are also the tipping point of relationships I and II. So LRDs ranging from 0.30 to 0.45 in increments of 0.05 require further discussion to determine the specific LRD classification threshold.

Table 3 shows the model training and validation results using different LRD thresholds such as 0.30, 0.35, 0.40, and 0.45 to develop the LRD classification model according to the GA-ANN algorithm. Model I corresponds to the algorithm developed for cases higher than the LRD threshold, and model II corresponds to the algorithm developed for cases less than the LRD threshold; i.e. model I used instantaneous daytime MODIS observations to estimate the daily average R_n, and model II used instantaneous nighttime MODIS observations to estimate daily average R_n. The R^2 and RMSE values were mainly applied to evaluate model performance because their bias values were similar. The biggest bias difference among various models was only 0.25 W/m^2 for the training result and 0.45 W/m^2 for the validation result (Table 3). Considering the training results as shown in Table 3, model I developed under an LRD classification threshold of 0.3 performed best with an R^2 of 0.86 and an RMSE of 22.55 W/m^2. Model I under diverse LRD thresholds had a comparable performance for the validation dataset. Model II developed under an LRD classification threshold of 0.3 had the highest accuracy for the training (R^2 = 0.5; RMSE = 14.95 W/m^2) and validation (R^2 = 0.51; RMSE = 15.04 W/m^2) datasets (Table 3). Considering the accuracy of models I and II, the LRD classification threshold was determined to be 0.3. Relationships I and II had R^2 values of 0.87 and 0.97, respectively, under an LRD threshold of 0.3. The following section of this study focuses on the LRD classification model developed using an LRD threshold of 0.3.

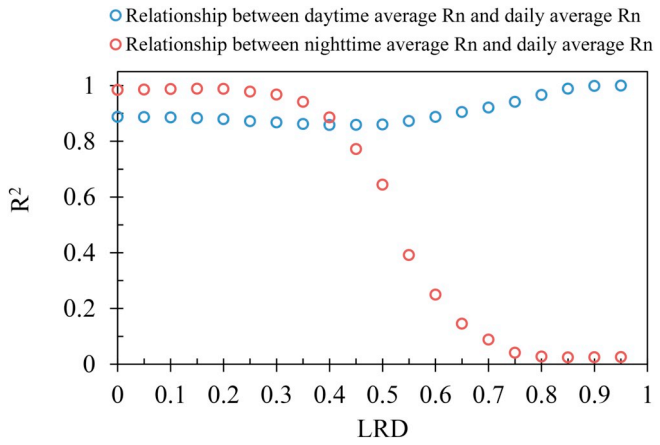

Fig. 4. R^2 between the daytime (nighttime) average R_n and daily average R_n when the dataset is divided into two groups using the predefined LRD threshold.

Table 3
Model training and validation results under different LRD classification threshold. Model I was developed under higher LRD values, and model II was developed under lower LRD values.

LRD	Model	Model training			Model validation		
		R^2	RMSE (W/m^2)	bias (W/m^2)	R^2	RMSE (W/m^2)	bias (W/m^2)
0.30	Model I	0.86	22.55	0.26	0.85	23.66	0.27
	Model II	0.5	14.95	−0.26	0.51	15.04	−0.08
0.35	Model I	0.86	23.14	0.16	0.85	23.51	0.00
	Model II	0.42	16.18	−0.06	0.42	16.14	0.37
0.40	Model I	0.85	23.56	0.27	0.85	23.64	0.45
	Model II	0.45	15.91	−0.13	0.41	16.27	0.09
0.45	Model I	0.85	24.15	0.32	0.85	24.01	0.12
	Model II	0.49	15.49	−0.01	0.49	15.54	0.06

3.3. Performance of the LRD classification model

The LRD classification model was proposed via a GA-ANN algorithm, where models I and II have 40 neurons each. The training and validation results of the LRD classification model are shown in Fig. 5. The training results of model I had an R^2 of 0.86, an RMSE of 22.55 W/m^2, and a bias of 0.26 W/m^2 (Fig. 5a). These values were 0.85, 23.66 W/m^2, and 0.27 W/m^2 (Fig. 5c), respectively, for the validation results. The model II training R^2, RMSE, and bias values were 0.5, 14.95 W/m^2, and −0.26 W/m^2 (Fig. 5b), respectively; and the model II validation R^2, RMSE, and bias values were 0.51, 15.04 W/m^2, and −0.08 W/m^2 (Fig. 5d), respectively. For models I and II, the R^2 values of the training process were nearly equal to that of the validation process and the RMSE values of the training process were lower than the validation process. In the training and validation processes, there was no significant difference in the bias for models I and II.

According to the scatter plots shown in Fig. 5, the GA-ANN algorithm showed satisfactory performance for establishing the LRD classification model in estimating the all-sky daily average R_n. GA-ANN inherits the merits of ANN and improves its performance. Compared with ANN, the main advantage of GA-ANN is the higher prediction accuracy, which has been demonstrated in previous studies (Armaghani et al., 2018; Irani and Nasimi, 2011; Mohamad et al., 2017). ANN validation results for model I had an R^2 of 0.83, an RMSE of 24.93 W/m^2, and a bias of 0.83 W/m^2, and these values were 0.40, 16.80 W/m^2, and −1.20 W/m^2 for the R^2, RMSE, and bias, respectively, in model II. Thus, GA-ANN also outperformed ANN for estimating daily average R_n.

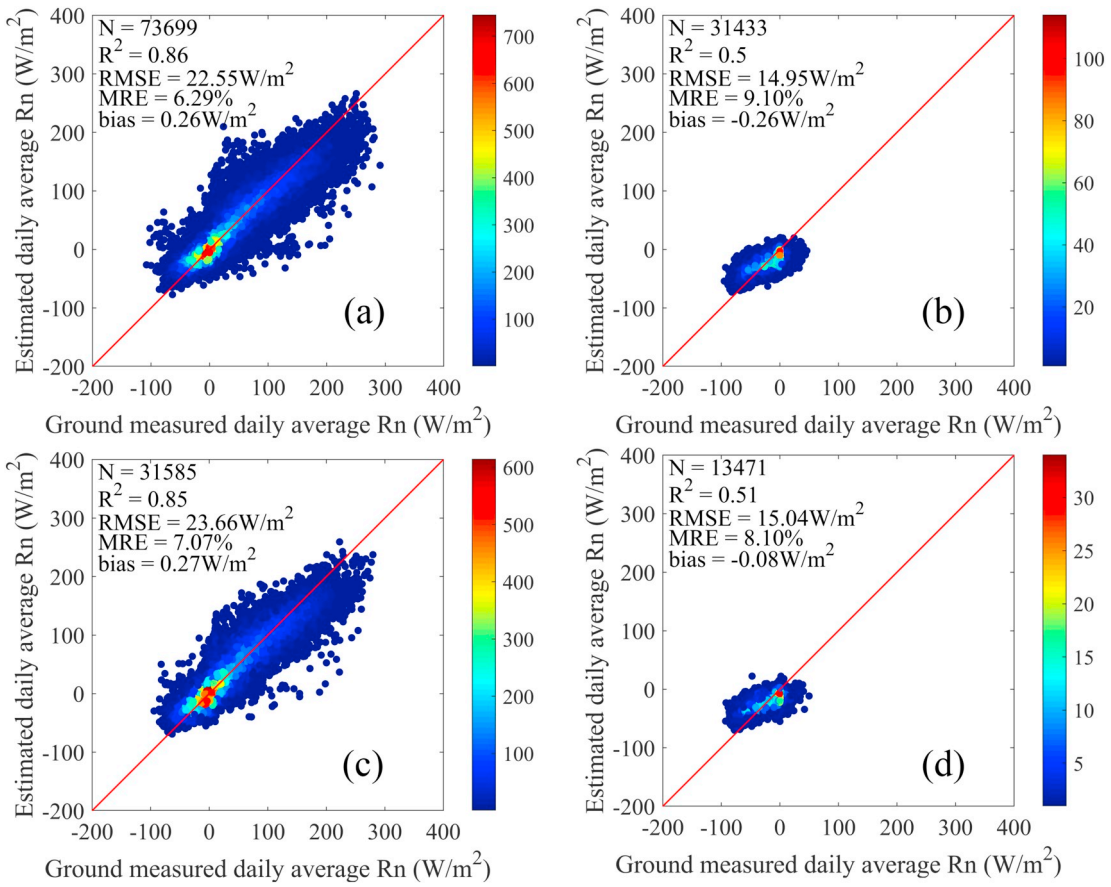

Fig. 5. GA-ANN model training and validation results under a LRD classification threshold of 0.3. (a) Model training result for model I; (b) model training result for model II; (c) model validation result for model I; (d) model validation result for model II. Model I corresponds to the algorithm developed under the cases that are higher than the LRD threshold of 0.3, and model II corresponds to the algorithm developed under the cases that are less than the LRD threshold of 0.3. Note that the color bar represents data density.

Note that we focus on the R_n retrieval scheme at high latitudes and test GA-ANN; however, the other machine learning algorithms such as support vector machine and random forest may also be applied.

For model validation, mean relative error (MRE) of model I and II were 7.07% and 8.10%, respectively. Compared to model I, model II had lower RMSE and bias and higher relative error. The range of daily average R_n is likely to increase with daytime length, and thus the model II outputs relatively lower R_n estimates for short daytime days. The accuracy of model I was mainly dependent on shortwave radiation, while model II performance was determined by longwave radiation. Previous studies have demonstrated that shortwave radiation could be accurately estimated using in situ data and matched satellite TOA observations (Hao et al., 2019; Jiang et al., 2019; Wei et al., 2019). However, so far, remote sensing estimation of longwave radiation under all-sky conditions is a significant challenge (Cheng et al., 2017; Wang et al., 2018; Zhou et al., 2018; Zhou et al., 2019). The aforementioned discussions provides the basis for model II having lower bias and RMSE but higher relative error. Wang et al. (2009) used hybrid model to estimate longwave net radiation under clear-sky conditions and evaluated model performance at six Surface Radiation Budget (SURFRAD) sites, and finding that RMSEs were close to 20 W/m^2. Guo et al. (2018) developed a machine learning model to estimate longwave net radiation under cloudy-sky conditions from shortwave net radiation, where the validation results at 24 sites had a bias of 0.01 W/m^2 and an RMSE of 26.10 W/m^2. Although we focus on R_n retrieval, the outputs of model II were mainly contributed by longwave net radiation (R^2 = 0.97), and validation results of model II (RMSE = 15.04 W/m^2, bias = −0.08 W/m^2) were slightly better than these studies. Although model II has satisfactory overall performance, it should be noted that model II may not be able to provide accurate estimates for the extreme cases with R_n values above 0 W/m^2 and close to −100 W/m^2, owing to a lack of sufficient training data that fell into the extreme value ranges. Recently, some new techniques have been introduced to estimate all-sky longwave radiation using additional auxiliary variables (e.g., Wang et al., 2019; Wang et al., 2020), which could be further evaluated and properly tuned at high latitudes to improve the accuracy of model II for extreme cases. Considering the unfeasibility of hybrid model and shortwave net radiation based model, model II shows potential and is easy to implement to estimate R_n under short daytime days.

MODIS cloud product (MOD035/MYD035) was used to discuss model performance for days dominated by clear-sky or cloudy-sky. MOD035/MYD035 provides four cloud detection confidence levels, namely, confident clear, probably clear, uncertain clear, and cloudy to each image pixel. Uncertain clear and cloudy pixels were labeled as cloudy, and confident clear and probably clear pixels were labeled as clear (Ying et al., 2019). Proportions of cloudy MODIS observations to total observation frequency were then calculated within one day. Table 4 presents the validation results of models I and II for different elevations, land cover types, and proportions of cloudy MODIS observations. These results indicate that model performance was not linked with elevation changes. With the except of barren land, validation results of models I and II for different land cover types were close. Models I and II over barren land performed slightly poorly than other land cover types. Shortwave/longwave net radiation retrieval models have been found to have lower accuracy at sites covered by barren land (Wang et al., 2009; Wang et al., 2015a, 2015b; Guo and Cheng, 2018), and such issues are also found in this study. This may be because of the high albedo and low specific heat capacity in barren areas (Diak et al.,

Table 4
Validation results of models I and II for different elevations, land cover types, and proportions of cloudy MODIS observations.

Group	Model I		Model II	
	RMSE (W/m^2)	bias (W/m^2)	RMSE (W/m^2)	bias (W/m^2)
Elevation (m)				
< 500	24.77	−0.25	14.73	−0.39
> 500 to 1000	21.58	−0.68	17.86	0.32
> 1000	18.02	0.69	16.38	0.57
Land cover types				
Forest	24.77	−1.69	16.82	0.29
Shrubland	27.10	1.15	12.30	−0.03
Grassland	23.16	1.93	12.43	−0.88
Wetland	19.16	0.40	13.49	−0.09
Ice/Snow	20.45	−0.35	17.28	0.21
Barren	27.85	−3.24	17.95	−1.59
Proportion of cloudy MODIS observations (100%)				
< 30	23.72	−0.12	16.46	3.02
> 30 to 60	25.67	−1.16	16.64	2.60
> 60	22.28	0.66	15.33	−1.46

2000; Guo and Cheng, 2018). Note that cloud detection products pose great uncertainty at high latitudes because of issues in distinguishing between cloud, snow, or ice (Zhu and Woodcock, 2012; Stillinger et al., 2019), and so validation results for different proportions of cloudy MODIS observations were only treated as the supplementary analysis. Generally, there are no significant differences for days dominated by clear-sky or cloudy-sky conditions. Thus, it may be concluded that overall model performance was acceptable, and the accuracy for different conditions including elevations/land cover types/sky conditions were close or comparable.

Previous studies have demonstrated that multiple satellite observations could improve the accuracy of estimating radiation flux components at a daily scale (Wang et al., 2015b; Wang et al., 2010). We used instantaneous MODIS observation to estimate the daily average R_n; therefore, multiple MODIS observations at high latitudes during one day correspond to multiple daily average R_n estimates. Final daily average R_n estimates were averaged from multiple daily average R_n estimates. Fig. 6 shows the relationship between the model error and MODIS observation frequency. The error largely decreased with the increase of MODIS observation frequency for model I. Compared with model I, the absolute error of model II presents a slight decrease with increasing MODIS observation frequency. Absolute errors of the R_n estimates from model II, ranging from −50 to 50 W/m^2, were relatively lower. Therefore, the contribution of MODIS observation frequency on the decreased error was less evident with a weak trend. As the observation frequency of MODIS and other polar-orbiting satellites is dependent on the latitude, lower latitudes achieved less MODIS overpasses. Wang et al. (2015b) recommended that combing the use of geostationary and polar-orbiting satellite datasets would help improve the accuracy of estimating daily average radiation fluxes. Note that invalid MODIS observations such as filling and abnormal data records were removed prior to model development. MODIS observation frequency histograms for models I and II are shown in Fig. 7. As for model I, the valid MODIS observation frequency had a mean value of 4.3 and most of these values (70.83%) were greater than 2. The corresponding values for model II, were 6 and 82.35%, respectively, indicating that polar orbiting contributes more valuable information in estimating the daily average R_n at high latitudes. Fig. 6 shows two interesting phenomena. First, the errors show a steady trend when the MODIS observation frequency increased to 14 for model I. This may be because the satellite overpasses 14 times per day were adequate to capture the diurnal cycle of R_n over high latitudes. This finding provides valuable information in determining the remote sensing data volume of estimating daily average R_n from multi-source satellites. Second, the clustering points occur around an error of zero when the valid MODIS observation frequency ranged from two to four. Stable weather conditions resulted in that limited satellite observation frequency still achieved the estimation of daily average R_n with high accuracy (Wang et al., 2010). On the other hand, most points concentrated around an error of zero indicated that the LRD classification model had good robustness. It has been demonstrated that the machine learning algorithm is a potential solution to estimate cloud parameters such as cloud top height and temperature using satellite observation (Håkansson et al., 2018; Min et al., 2020). For cloudy-conditions, those cloud parameters are the main factors controlling longwave balance at the surface (Wang et al., 2018). Thus, the proposed model II in this study had acceptable results in estimating the daily average R_n under all-sky conditions.

We also developed model I only using shortwave bands to estimate R_n; model performance was evaluated as shown in Fig. 8. The training and validation results indicate that model I, without MODIS longwave bands, had a larger bias value when the daily average R_n was greater than 200 W/m^2, which was consistent with previous studies (Wang et al., 2015a). Compared with model I that used a combination of MODIS shortwave and longwave bands, the validation results had decreased R^2 (0.82), increased RMSE (25.73 W/m^2) and bias (1.51 W/m^2). As the number of point pairs was large, the overall statistical indicators changed slightly. This is because the relationship between the R_n and shortwave net radiation would deteriorate at times, and the contribution of longwave radiation fluxes on R_n could not be fully accounted. Overall, our results suggest that the longwave information plays an important role in estimating R_n.

3.4. Model application over the high latitudes

The time series for the daily average R_n validation results in 2014 at six sites along a gradient of varying latitude are shown in Fig. 9. It is evident that the estimated R_n could sufficiently capture seasonal changes. The validation results at the six sites are acceptable with an RMSE of less than 23.86 W/m^2, a bias of less than −5.56 W/m^2, and an R^2 of more than 0.88. The six examples show that the LRD classification model developed using the GA-ANN algorithm performs well along the varying latitude. Overall, the remote sensing estimates of the daily average R_n were close to ground measurements. Furthermore, there were no large bias values in the R_n estimates for models I and II (Fig. 9), and the R_n estimates were continuous when the LRD threshold value was near 0.3.

As shown in Fig. 10, the LRD classification model was further applied to the real MODIS images to map the daily average R_n at high latitudes on March 23, July 20, September 23, and December 25, 2014. The high latitudes had significantly varying LRD values in these four seasons. Model I was mainly used for July 20, 2014, and model II was mainly used for December 25, 2014. The daily average R_n derived from the CERES-SYN product for the same day was also presented in Fig. 10 to compare the overall spatial distributions. There were significant differences with respect to the number of pixels from our estimates and CERES product. There were approximately 8,705,863 pixels in the R_n mapping estimated from our GA-ANN LRD classification model, approximately 2291 times that from CERES-SYN product (approximately 3800 pixels).

Fig. 10 shows that the R_n estimates from MODIS and CERES have similar spatial distribution patterns in different seasons. There are lower R_n estimates in relatively higher latitude regions. Mappings of daily average R_n imply that our proposed models have potential values for estimating daily 1 km R_n at high latitudes. R_n estimates on February 28, 2014 were also mapped (Fig. 11). In this study, two R_n retrieval models were built based on the LRD threshold value of 0.3. On February 28, 2014, if latitude was greater than 76.7°, the LRD value was less than 0.3, while if latitude was less than 76.7°, the LRD value was greater than 0.3. As shown in Fig. 11, R_n estimates were also continuous when the LRD value was near 0.3. Besides, R_n estimates from MODIS and

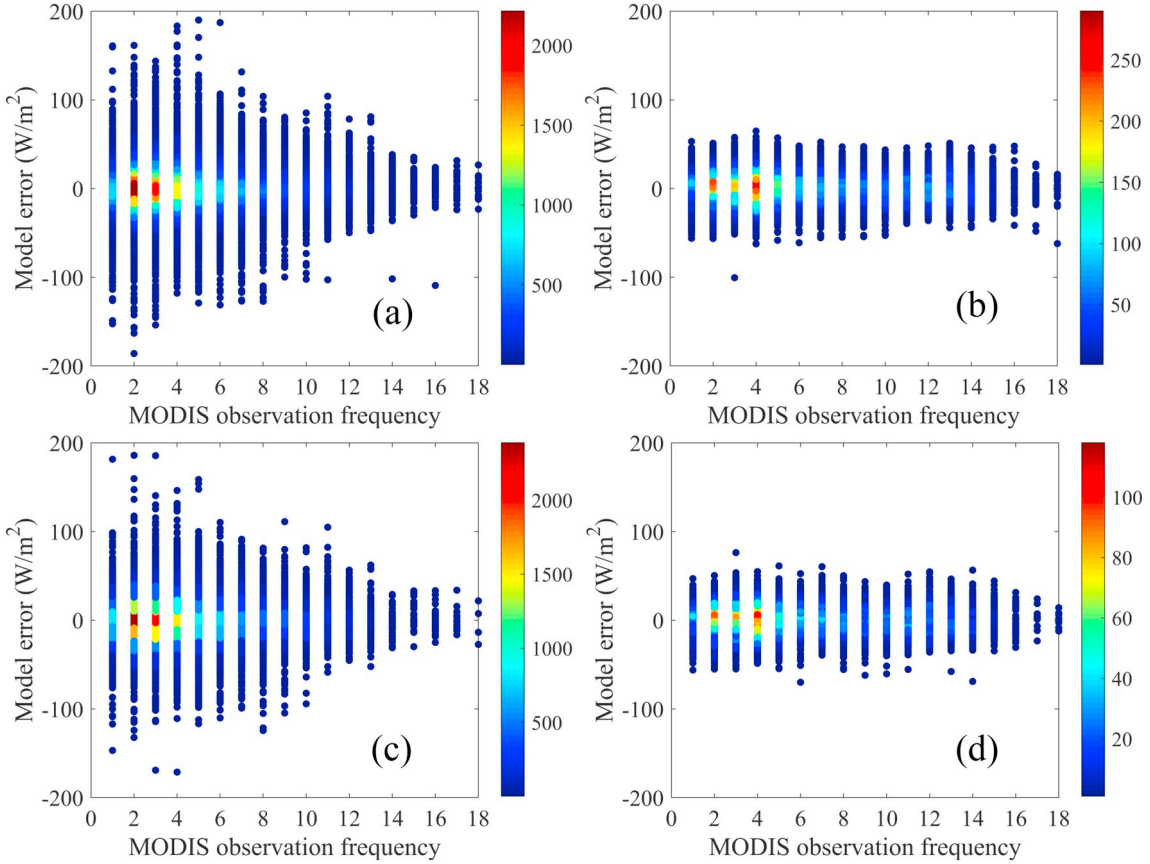

Fig. 6. Scatter plots of model training error, model validation error, and MODIS observation frequency. (a) Model training error and MODIS observation frequency for model I; (b) model training error and MODIS observation frequency for model II; (c) model validation error and MODIS observation frequency for model I; (d) model validation error and MODIS observation frequency for model II. Note that the color bar represents data density.

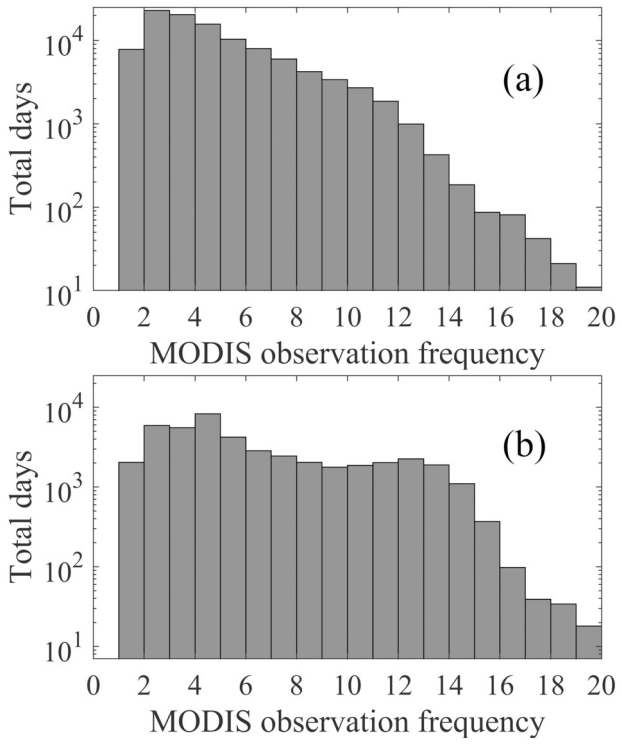

Fig. 7. Histogram of MODIS observation frequency. (a) Histogram of model I; (b) histogram of model II.

CERES also have a similar spatial distribution pattern. This indicates that the chosen LRD threshold value is reasonable. Compared with the CERES product, the R_n estimates from MODIS provided more details due to a much higher spatial resolution. There is an abnormal high-value R_n area in central Greenland (Fig. 10(h)), which may be due to the poor precision of CERES R_n over Greenland (Jia et al., 2016). However, MODIS-estimated R_n had smooth changes in this area.

These differences between MODIS and CERES are partly due to the disparity of the algorithm, data source, and many other factors. R_n is affected by both land surface and atmospheric conditions. The proposed algorithm was developed using extensive matched pairs between in situ R_n data and MODIS TOA observations. Thus, the algorithm performance may degrade in areas where the land surface and atmospheric conditions are not included in our dataset. Actually, we have tried our best to collect in situ measured R_n data. There are limitations that remain for the proposed algorithm. Further work will be done to improve the estimation of longwave radiation at high latitudes in the future. However, the merits of our algorithm include its independence from other auxiliary data, great maneuverability, and the generation of R_n results with 1 km spatial resolution. Finally, the solution of model I development and implementation proposed in this study may still be suitable for the mid and low latitudes. However, the employed satellite should be changed to geostationary satellite such as GOES-16, MSG-1, and Himawari-8. The remote sensing algorithm for estimating all-sky daily average R_n provides the potential for spatio-temporal analysis of SEB over high latitudes such as Greenland and other ice-covered areas.

4. Conclusion

R_n is a significant parameter driving various land surface processes

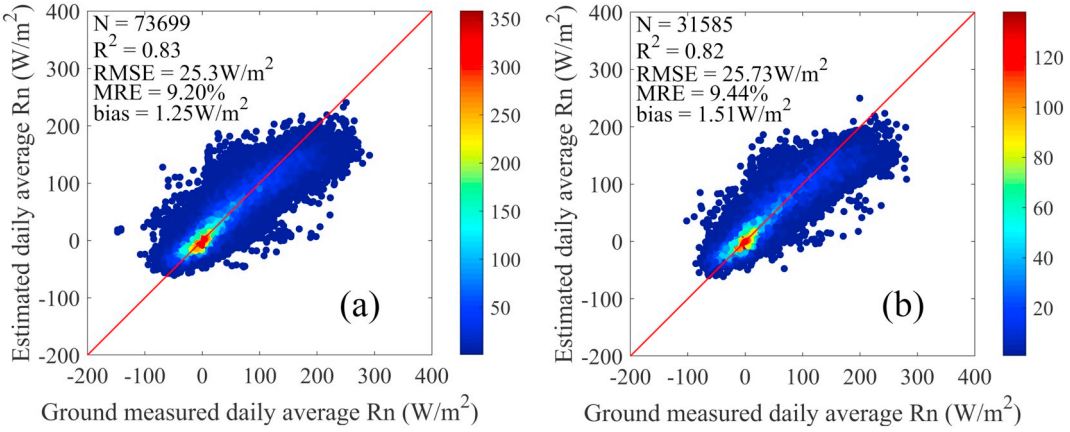

Fig. 8. GA-ANN model training and validation results using only shortwave bands of MODIS for model I. Note that the color bar represents data density.

and quantifying SEB status; thus, accurate estimation of R_n is of great importance. In this study, we focused on the estimation of the daily average R_n from MODIS data at high latitudes. A hybrid machine learning model, the GA-ANN algorithm, was adopted to estimate the daily average R_n because of the known limitations of existing methods at high latitudes. To further improve the R_n, LRD values were introduced to distinguish the different contributions of daytime and nighttime R_n to the daily average R_n. Based on sensitivity analysis, it was found that an LRD value of 0.3 was the best threshold to develop the LRD classification model. The LRD classification model, including models I and II, was employed to estimate the daily average R_n under all LRD conditions. Model I had an R^2 of 0.85, an RMSE of 23.66 W/m^2, and a bias of 0.27 W/m^2 for the validation dataset, whereas these values were 0.51, 15.04 W/m^2, and − 0.08 W/m^2 for model II. Errors of the R_n estimates decreased with increasing MODIS observation frequency. The contribution of longwave radiation fluxes on R_n should be carefully accounted by inputting MODIS longwave bands in the GA-ANN model. Time series for the validation results of the daily average R_n in 2014 at six sites along the varying latitude indicated that the estimated R_n from MODIS sufficiently captured seasonal changes, with an RMSE of less than 23.86 W/m^2, a bias of less than −5.56 W/m^2, and an R^2 of more than 0.88. Application of the LRD classification model to real MODIS images to map the daily average R_n over high latitudes on March 23, July 20, September 23, and December 25, 2014, had a similar spatial distribution to the CERES product.

Overall, the LRD classification model that was developed based on the GA-ANN algorithm is a feasible scheme to estimate the daily average R_n with 1 km spatial resolution at high latitudes. The model proposed in this study needs no high-level surface and atmosphere parameter products or auxiliary data and only uses MODIS L1B products. Thus, the proposed approach demonstrated the potential for generating long-term daily average R_n products with MODIS data. This is a very important supplement to existing data sources for climate change applications at high latitudes. The R_n products will be available in the near future.

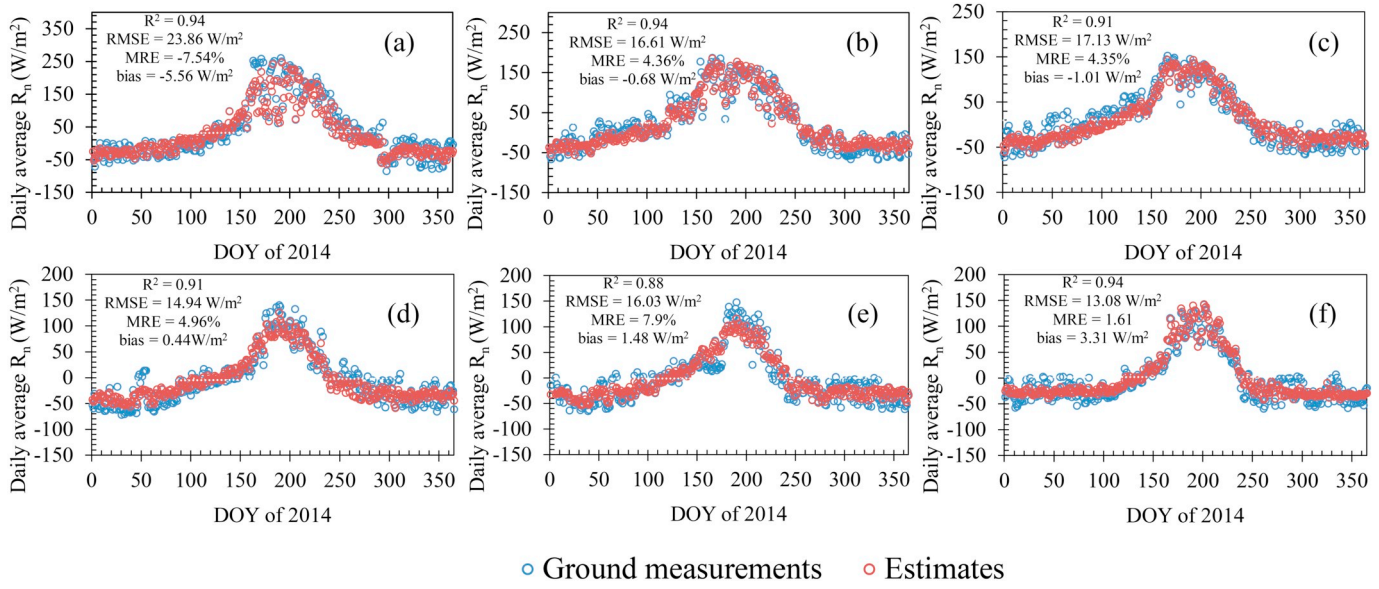

Fig. 9. Time series for daily average R_n in 2014 at six sites along a gradient of varying latitude. The latitude and longitude of six sites are: (a) 61.0308°, −46.8493°; (b) 64.4822°, −49.5358°; (c) 67.0955°, −49.9513°; (d) 72.8878°, −53.5783°; (e) 76.3998°, −68.2665°; (f) 79.9108°, −24.0828°. Altitude of the six sites are 280, 530, 670, 940, 570, and 370 m, respectively.

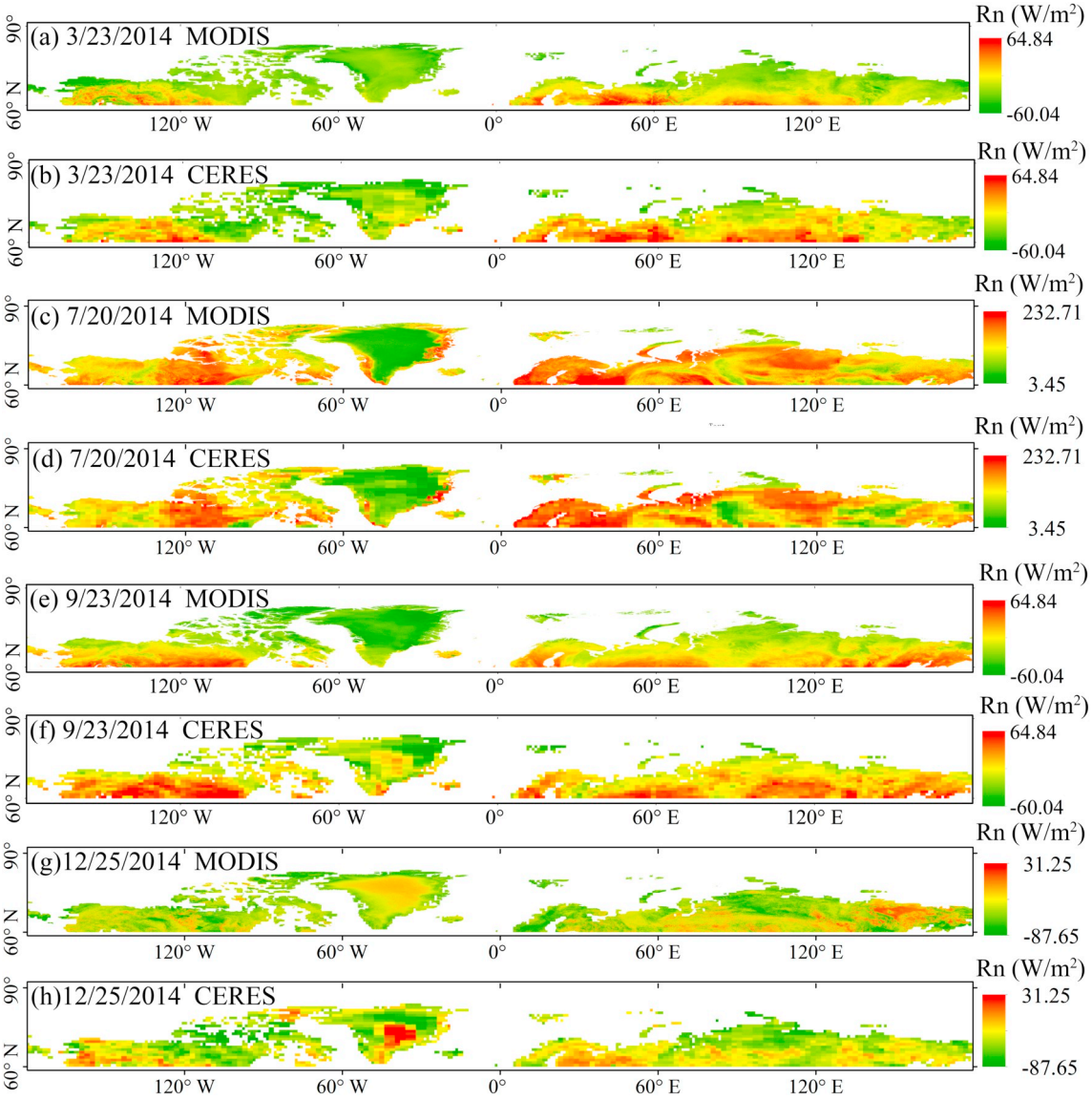

Fig. 10. Mapping of daily average R_n at high latitudes on March 23, July 20, September 23, and December 25, 2014. (a), (c), (e), and (g) are R_n estimates derived from MODIS images at 1 km spatial resolution on March 23, July 20, September 23, and December 25, 2014, respectively. (b), (d), (f), and (h) are R_n estimates derived from CERES product at 1° spatial resolution on March 23, July 20, September 23, and December 25, 2014, respectively.

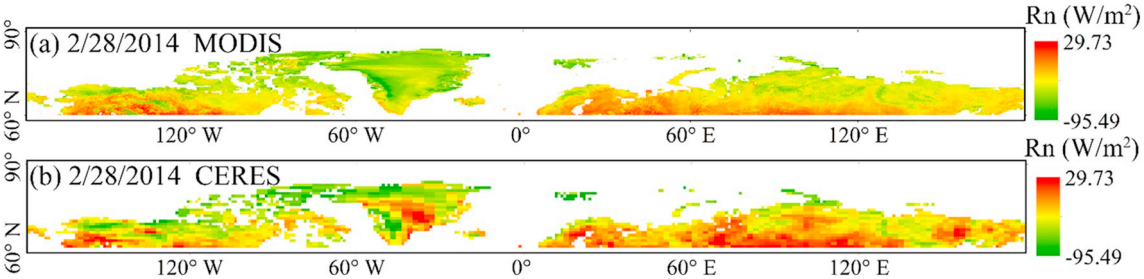

Fig. 11. Mapping of daily average R_n at high latitudes on February 28, 2014. (a) R_n estimates derived from MODIS at 1 km spatial resolution on February 28, 2014. (b) R_n estimates derived from CERES product at 1° spatial resolution on February 28, 2014. LRD is 0.3 near latitude 76.7°.

CRediT authorship contribution statement

Jiang Chen: Methodology, Data curation, Writing - original draft.**Tao He:**Conceptualization, Methodology, Writing - review & editing.**Bo Jiang:**Methodology, Writing - review & editing.**Shunlin Liang:**Supervision, Writing - review & editing.

Acknowledgments

This work is supported by the National Natural Science Foundation of China (Grant no. 41771379), the Chinese National Earth System Science Data Center, and Chinese Grand Research Program on Climate Change and Response under project 2016YFA0600101. We thank the CERES team for providing the CERES-SYN product freely download via the website (https://ceres.larc.nasa.gov/products-info.php?product=SYN1deg). We thank MODIS team for offering Level-1B product downloaded from https://search.earthdata.nasa.gov/search. The present study used in situ observed radiation data were downloaded from EFDC (http://www.europe-fluxdata.eu/), FLUXNET (https://fluxnet.fluxdata.org/), AmeriFlux (https://ameriflux.lbl.gov/), BSRN (https://bsrn.awi.de/), CEOP (https://www.eol.ucar.edu/field_projects/ceop), PROMICE (http://www.promice.org/), IMAU (http://www.projects.science.uu.nl/iceclimate/), and AsiaFlux (https://db.cger.nies.go.jp/asiafluxdb/). We thank the mentioned observation network for providing invaluable field measurements. We would like to thank the four anonymous reviewers for their valuable comments and suggestions.

Declaration of competing interest

The authors declare that they have no known competing financial interests or personal relationships that could have appeared to influence the work reported in this paper.

References

Alados, I., Foyo-Moreno, I., Olmo, F.J., Alados-Arboledas, L., 2003. Relationship between net radiation and solar radiation for semi-arid shrub-land. Agric. For. Meteorol. 116, 221–227.

Amatya, P.M., Ma, Y., Han, C., Wang, B., Devkota, L.P., 2015. Estimation of net radiation flux distribution on the southern slopes of the central Himalayas using MODIS data. Atmos. Res. 154, 146–154.

Armaghani, D.J., Hasanipanah, M., Mahdiyar, A., Majid, M.Z.A., Amnieh, H.B., Tahir, M.M., 2018. Airblast prediction through a hybrid genetic algorithm-ANN model. Neural Comput. & Applic. 29, 619–629.

Babar, B., Graversen, R., Boström, T., 2019. Solar radiation estimation at high latitudes: assessment of the CMSAF databases, ASR and ERA5. Sol. Energy 182, 397–411.

Babar, B., Luppino, L.T., Boström, T., Anfinsen, S.N., 2020. Random forest regression for improved mapping of solar irradiance at high latitudes. Sol. Energy 198, 81–92.

Bastiaanssen, W., Noordman, E., Pelgrum, H., Davids, G., Thoreson, B., Allen, R., 2005. SEBAL model with remotely sensed data to improve water-resources management under actual field conditions. J. Irrig. Drain. Eng. 131, 85–93.

Bisht, G., Bras, R.L., 2010. Estimation of net radiation from the MODIS data under all sky conditions: Southern Great Plains case study. Remote Sens. Environ. 114, 1522–1534.

Bisht, G., Venturini, V., Islam, S., Jiang, L., 2005. Estimation of the net radiation using MODIS (Moderate Resolution Imaging Spectroradiometer) data for clear sky days. Remote Sens. Environ. 97, 52–67.

Box, J.E., Colgan, W.T., Wouters, B., Burgess, D.O., O'Neel, S., Thomson, L.I., Mernild, S.H., 2018. Global sea-level contribution from Arctic land ice: 1971–2017. Environ. Res. Lett. 13, 125012.

van den Broeke, M., Smeets, P., Ettema, J., Munneke, P.K., 2008. Surface radiation balance in the ablation zone of the West Greenland ice sheet. Journal of Geophysical Research: Atmospheres 113.

Brown, P.T., Caldeira, K., 2017. Greater future global warming inferred from Earth's recent energy budget. Nature 552, 45–50.

Cheng, J., Liang, S., 2016. Global estimates for high-spatial-resolution clear-sky land surface upwelling longwave radiation from MODIS data. IEEE Trans. Geosci. Remote Sens. 54, 4115–4129.

Cheng, J., Liang, S., Wang, W., Guo, Y., 2017. An efficient hybrid method for estimating clear-sky surface downward longwave radiation from MODIS data. Journal of Geophysical Research: Atmospheres 122, 2616–2630.

Deo, R.C., Şahin, M., Adamowski, J.F., Mi, J., 2019. Universally deployable extreme learning machines integrated with remotely sensed MODIS satellite predictors over Australia to forecast global solar radiation: a new approach. Renew. Sust. Energ. Rev. 104, 235–261.

Diak, G.R., Bland, W.L., Mecikalski, J.R., Anderson, M.C., 2000. Satellite-based estimates of longwave radiation for agricultural applications. Agric. For. Meteorol. 103, 349–355.

Dickinson, R.E., Oleson, K.W., Bonan, G., Hoffman, F., Thornton, P., Vertenstein, M., Yang, Z.-L., Zeng, X., 2006. The community land model and its climate statistics as a component of the community climate system model. J. Clim. 19, 2302–2324.

Duarte, H.F., Dias, N.L., Maggiotto, S.R., 2006. Assessing daytime downward longwave radiation estimates for clear and cloudy skies in Southern Brazil. Agric. For. Meteorol. 139, 171–181.

Fu, Q., Liou, K.N., 1993. Parameterization of the radiative properties of cirrus clouds. J. Atmos. Sci. 50, 2008–2025.

Ghimire, S., Deo, R.C., Downs, N.J., Raj, N., 2018. Self-adaptive differential evolutionary extreme learning machines for long-term solar radiation prediction with remotely-sensed MODIS satellite and reanalysis atmospheric products in solar-rich cities. Remote Sens. Environ. 212, 176–198.

Gui, S., Liang, S.L., Li, L., 2010. Evaluation of satellite-estimated surface longwave radiation using ground-based observations. J. Geophys. Res.-Atmos. 115.

Guo, Y., Cheng, J., 2018. Feasibility of estimating cloudy-sky surface Longwave net radiation using satellite-derived surface shortwave net radiation. Remote Sens. 10, 596.

Gupta, S.K., Kratz, D.P., Wilber, A.C., Nguyen, L.C., 2004. Validation of parameterized algorithms used to derive TRMM–CERES surface radiative fluxes. J. Atmos. Ocean. Technol. 21, 742–752.

Gusain, H., Singh, D.K., Mishra, V., Arora, M., 2019. Estimation of net radiation flux of Antarctic ice sheet in east Dronning Maud Land, Antarctica, during clear sky days using remote sensing and meteorological data. Remote Sensing in Earth Systems Sciences 1–11.

Håkansson, N., Adok, C., Thoss, A., Scheirer, R., Hörnquist, S., 2018. Neural network cloud top pressure and height for MODIS. Atmospheric Measurement Techniques 11, 3177–3196.

Hall, D., Cullather, R., DiGirolamo, N., Comiso, J., Medley, B., Nowicki, S., 2018. A multilayer surface temperature, surface albedo, and water vapor product of Greenland from MODIS. Remote Sens. 10, 555.

Han, D., Kwong, T., Li, S., 2007. Uncertainties in real-time flood forecasting with neural networks. Hydrological Processes: An International Journal 21, 223–228.

Hao, D., Asrar, G.R., Zeng, Y., Zhu, Q., Wen, J., Xiao, Q., Chen, M., 2019. Estimating hourly land surface downward shortwave and photosynthetically active radiation from DSCOVR/EPIC observations. Remote Sens. Environ. 232, 111320.

He, T., Liang, S., Yu, Y., Wang, D., Gao, F., Liu, Q., 2013. Greenland surface albedo changes in July 1981–2012 from satellite observations. Environ. Res. Lett. 8, 044043.

He, T., Liang, S., Wang, D., Shi, Q., Goulden, M.L., 2015. Estimation of high-resolution land surface net shortwave radiation from AVIRIS data: algorithm development and preliminary results. Remote Sens. Environ. 167, 20–30.

Holland, J., 1975. Adaptation in natural and artificial systems: An introductory analysis with applications to biology, control and artificial intelligence. University of Michigan Press, Ann Arbor, MI.

Hu, B., Wang, Y., Liu, G., 2011. Relationship between net radiation and broadband solar radiation in the Tibetan Plateau. Adv. Atmos. Sci. 29, 135–143.

Huang, G., Li, X., Ma, M., Li, H., Huang, C., 2016. High resolution surface radiation products for studies of regional energy, hydrologic and ecological processes over Heihe river basin, northwest China. Agric. For. Meteorol. 230–231, 67–78.

Irani, R., Nasimi, R., 2011. Evolving neural network using real coded genetic algorithm for permeability estimation of the reservoir. Expert Syst. Appl. 38, 9862–9866.

Jia, A., Jiang, B., Liang, S., Zhang, X., Ma, H., 2016. Validation and spatiotemporal analysis of CERES surface net radiation product. Remote Sens. 8, 90.

Jia, A., Liang, S., Jiang, B., Zhang, X., Wang, G., 2018. Comprehensive assessment of global surface net radiation products and uncertainty analysis. Journal of Geophysical Research: Atmospheres 123, 1970–1989.

Jiang, B., Zhang, Y., Liang, S., Wohlfahrt, G., Arain, A., Cescatti, A., Georgiadis, T., Jia, K., Kiely, G., Lund, M., Montagnani, L., Magliulo, V., Ortiz, P.S., Oechel, W., Vaccari, F.P., Yao, Y., Zhang, X., 2015. Empirical estimation of daytime net radiation from shortwave radiation and ancillary information. Agric. For. Meteorol. 211–212, 23–36.

Jiang, B., Liang, S., Ma, H., Zhang, X., Xiao, Z., Zhao, X., Jia, K., Yao, Y., Jia, A., 2016. GLASS daytime all-wave net radiation product: algorithm development and preliminary validation. Remote Sens. 8, 222.

Jiang, B., Liang, S., Jia, A., Xu, J., Zhang, X., Xiao, Z., Zhao, X., Jia, K., Yao, Y., 2018. Validation of the surface daytime net radiation product from version 4.0 GLASS product suite. IEEE Geosci. Remote Sens. Lett. 1–5.

Jiang, H., Lu, N., Qin, J., Tang, W., Yao, L., 2019. A deep learning algorithm to estimate hourly global solar radiation from geostationary satellite data. Renew. Sust. Energ. Rev. 114, 109327.

Jung, M., Koirala, S., Weber, U., Ichii, K., Gans, F., Camps-Valls, G., Papale, D., Schwalm, C., Tramontana, G., Reichstein, M., 2019. The FLUXCOM ensemble of global land-atmosphere energy fluxes. Sci Data 6, 74.

Kaminsky, K.Z., Dubayah, R., 1997. Estimation of surface net radiation in the boreal forest and northern prairie from shortwave flux measurements. Journal of Geophysical Research: Atmospheres 102, 29707–29716.

Kato, S., Yamaguchi, Y., 2005. Analysis of urban heat-island effect using ASTER and ETM + data: separation of anthropogenic heat discharge and natural heat radiation from sensible heat flux. Remote Sens. Environ. 99, 44–54.

Kayarvizhy, N., Kanmani, S., Uthariaraj, R., 2013. Improving fault prediction using ANN-PSO in object oriented systems. International Journal of Computer Applications 73, 0975–8887.

Khajeh, M., Moghaddam, M.G., Shakeri, M., 2012. Application of artificial neural network in predicting the extraction yield of essential oils of Diplotaenia cachrydifolia by supercritical fluid extraction. J. Supercrit. Fluids 69, 91–96.

Kuang, W., Liu, A., Dou, Y., Li, G., Lu, D., 2018. Examining the impacts of urbanization on surface radiation using Landsat imagery. GIScience & Remote Sensing 1–23.

Kuipers Munneke, P., Smeets, C.J.P.P., Reijmer, C.H., Oerlemans, J., van de Wal, R.S.W.,

& van den Broeke, M.R. (2018). The K-transect on the western Greenland ice sheet: surface energy balance (2003–2016). Arct. Antarct. Alp. Res., 50, S100003.
Liang, S., Kustas, W., Schaepman-Strub, G., Li, X., 2010a. Impacts of climate change and land use changes on land surface radiation and energy budgets. IEEE Journal of Selected Topics in Applied Earth Observations and Remote Sensing 3, 219–224.
Liang, S., Wang, K., Zhang, X., Wild, M., 2010b. Review on estimation of land surface radiation and energy budgets from ground measurement, remote sensing and model simulations. IEEE Journal of Selected Topics in Applied Earth Observations and Remote Sensing 3, 225–240.
Liang, S., Wang, D., He, T., Yu, Y., 2019. Remote sensing of earth's energy budget: synthesis and review. International Journal of Digital Earth 12, 737–780.
Lippmann, R., 1987. An introduction to computing with neural nets. IEEE ASSP Mag. 4, 4–22.
Miller, N.B., Shupe, M.D., Lenaerts, J.T.M., Kay, J.E., de Boer, G., Bennartz, R., 2018. Process-based model evaluation using surface energy budget observations in Central Greenland. Journal of Geophysical Research: Atmospheres 123, 4777–4796.
Min, M., Li, J., Wang, F., Liu, Z., Menzel, W.P., 2020. Retrieval of cloud top properties from advanced geostationary satellite imager measurements based on machine learning algorithms. Remote Sens. Environ. 239, 111616.
Mira, M., Olioso, A., Gallego-Elvira, B., Courault, D., Garrigues, S., Marloie, O., Hagolle, O., Guillevic, P., Boulet, G., 2016. Uncertainty assessment of surface net radiation derived from Landsat images. Remote Sens. Environ. 175, 251–270.
Mohamad, E.T., Faradonbeh, R.S., Armaghani, D.J., Monjezi, M., Majid, M.Z.A., 2017. An optimized ANN model based on genetic algorithm for predicting ripping production. Neural Comput. & Applic. 28, 393–406.
Moukomla, S., Blanken, P.D., 2016. Estimating the Great Lakes net radiation using satellite remote sensing and MERRA reanalysis. International Journal of Digital Earth 10, 764–784.
Niu, X., Pinker, R.T., Cronin, M.F., 2010. Radiative fluxes at high latitudes. Geophys. Res. Lett. 37 (n/a-n/a).
Offerle, B., Grimmond, C., Oke, T.R., 2003. Parameterization of net all-wave radiation for urban areas. J. Appl. Meteorol. 42, 1157–1173.
Peng, Z., Letu, D.H., Wang, T., Shi, D.C., Zhao, C., Tana, G., Zhao, N., Dai, T., Tang, R., Shang, H., Shi, J., Chen, L., 2019. Estimation of shortwave solar radiation using the artificial neural network from Himawari-8 satellite imagery over China. J. Quant. Spectrosc. Radiat. Transf. 240, 1–8 106672.
Ramírez-Cuesta, J.M., Vanella, D., Consoli, S., Motisi, A., Minacapilli, M., 2018. A satellite stand-alone procedure for deriving net radiation by using SEVIRI and MODIS products. Int. J. Appl. Earth Obs. Geoinf. 73, 786–799.
Raschke, E., Bakan, S., Kinne, S., 2006. An assessment of radiation budget data provided by the ISCCP and GEWEX-SRB. Geophys. Res. Lett. 33.
Ryu, Y., Kang, S., Moon, S.-K., Kim, J., 2008. Evaluation of land surface radiation balance derived from moderate resolution imaging spectroradiometer (MODIS) over complex terrain and heterogeneous landscape on clear sky days. Agric. For. Meteorol. 148, 1538–1552.
Saini, L., Soni, M., 2002. Artificial neural network based peak load forecasting using Levenberg–Marquardt and quasi-Newton methods. IEE Proceedings-Generation, Transmission and Distribution 149, 578–584.
Stillinger, T., Roberts, D.A., Collar, N.M., Dozier, J., 2019. Cloud masking for Landsat 8 and MODIS Terra over snow-covered terrain: Error analysis and spectral similarity between snow and cloud. Water Resour. Res. 55, 6169–6184.
Toller, G., Isaacman, A., Kuyper, J., Geng, X., Xiong, J., 2009. MODIS Level 1B Product User's Guide for Level 1B Version 6.1. 0 (Terra) and Version 6.1. 1 (Aqua). MODIS Characterization Support Team (MCST).
Van As, D., 2011. Warming, glacier melt and surface energy budget from weather station observations in the Melville Bay region of northwest Greenland. J. Glaciol. 57, 208–220.
Van Den Broeke, M., Reijmer, C., Van De Wal, R., 2004. Surface radiation balance in Antarctica as measured with automatic weather stations. Journal of Geophysical Research: Atmospheres 109.
Vaughan, D.G., Doake, C., 1996. Recent atmospheric warming and retreat of ice shelves on the Antarctic Peninsula. Nature 379, 328.
Wang, W., Liang, S., 2009. Estimation of high-spatial resolution clear-sky longwave downward and net radiation over land surfaces from MODIS data. Remote Sens. Environ. 113, 745–754.
Wang, K., Wang, P., Li, Z., Cribb, M., Sparrow, M., 2007. A simple method to estimate actual evapotranspiration from a combination of net radiation, vegetation index, and temperature. J. Geophys. Res. 112.
Wang, W., Liang, S., & J. A. , A. (2009). Estimating high spatial resolution clear-sky land surface upwelling longwave radiation from MODIS data. IEEE Trans. Geosci. Remote Sens., 47, 1559–1570.
Wang, D., Liang, S., Liu, R., Zheng, T., 2010. Estimation of daily-integrated PAR from sparse satellite observations: comparison of temporal scaling methods. Int. J. Remote Sens. 31, 1661–1677.
Wang, T., Yan, G., Chen, L., 2012. Consistent retrieval methods to estimate land surface shortwave and longwave radiative flux components under clear-sky conditions. Remote Sens. Environ. 124, 61–71.
Wang, D., Liang, S., He, T., Shi, Q., 2015a. Estimating clear-sky all-wave net radiation from combined visible and shortwave infrared (VSWIR) and thermal infrared (TIR) remote sensing data. Remote Sens. Environ. 167, 31–39.
Wang, D., Liang, S., He, T., Shi, Q., 2015b. Estimation of daily surface shortwave net radiation from the combined MODIS data. IEEE Trans. Geosci. Remote Sens. 53, 5519–5529.
Wang, T., Shi, J., Yu, Y., Husi, L., Gao, B., Zhou, W., Ji, D., Zhao, T., Xiong, C., Chen, L., 2018. Cloudy-sky land surface longwave downward radiation (LWDR) estimation by integrating MODIS and AIRS/AMSU measurements. Remote Sens. Environ. 205, 100–111.
Wang, T., Shi, J., Ma, Y., Husi, L., Comyn-Platt, E., Ji, D., Zhao, T., Xiong, C., 2019. Recovering land surface temperature under cloudy skies considering the solar-cloud-satellite geometry: application to MODIS and Landsat-8 data. Journal of Geophysical Research: Atmospheres 124, 3401–3416.
Wang, T., Shi, J., Ma, Y., Letu, H., Li, X., 2020. All-sky longwave downward radiation from satellite measurements: general parameterizations based on LST, column water vapor and cloud top temperature. ISPRS J. Photogramm. Remote Sens. 161, 52–60.
Wei, Y., Zhang, X., Hou, N., Zhang, W., Jia, K., Yao, Y., 2019. Estimation of surface downward shortwave radiation over China from AVHRR data based on four machine learning methods. Sol. Energy 177, 32–46.
Weston, S.T., Bailey, W.G., McArthur, L.J.B., Hertzman, O., 2007. Interannual solar and net radiation trends in the Canadian Arctic. Journal of Geophysical Research: Atmospheres 112.
Wielicki, B.A., Barkstrom, B.R., Harrison, E.F., Lee III, R.B., Smith, G.L., Cooper, J.E., 1996. Clouds and the Earth's radiant energy system (CERES): an earth observing system experiment. Bull. Am. Meteorol. Soc. 77, 853–868.
Wild, M., Folini, D., Schär, C., Loeb, N., Dutton, E.G., König-Langlo, G., 2013. The global energy balance from a surface perspective. Clim. Dyn. 40, 3107–3134.
Ying, W., Wu, H., Li, Z., 2019. Net surface shortwave radiation retrieval using random forest method with MODIS/AQUA data. IEEE Journal of Selected Topics in Applied Earth Observations and Remote Sensing 1–8.
Zhang, X., Wang, D., Liu, Q., Yao, Y., Jia, K., He, T., Jiang, B., Wei, Y., Ma, H., Zhao, X., Li, W., Liang, S., 2019. An operational approach for generating the global land surface downward shortwave radiation product from MODIS data. IEEE Trans. Geosci. Remote Sens. 1–15.
Zhao, W., Li, Z.-L., Wu, H., Tang, B.-H., Zhang, X., Song, X., Zhou, G., 2013. Determination of bare surface soil moisture from combined temporal evolution of land surface temperature and net surface shortwave radiation. Hydrol. Process. 27, 2825–2833.
Zhao, L., Shen, Z., Li, C., Guo, M., Sun, Y., Gao, L., 2019. Evaluating the estimation of net radiation based on MODIS data and CoLM: a case study in the Tibetan plateau. IEEE Journal of Selected Topics in Applied Earth Observations and Remote Sensing 12, 460–470.
Zhong, L., Zou, M., Ma, Y., Huang, Z., Xu, K., Wang, X., Ge, N., Cheng, M., 2019. Estimation of downwelling shortwave and longwave radiation in the Tibetan Plateau under all-sky conditions. Journal of Geophysical Research: Atmospheres 124, 11086–11102.
Zhou, Y., Cess, R.D., 2001. Algorithm development strategies for retrieving the downwelling longwave flux at the Earth's surface. Journal of Geophysical Research: Atmospheres 106, 12477–12488.
Zhou, Y., Kratz, D.P., Wilber, A.C., Gupta, S.K., Cess, R.D., 2007. An improved algorithm for retrieving surface downwelling longwave radiation from satellite measurements. Journal of Geophysical Research: Atmospheres 112.
Zhou, X.-M., Tang, B.-H., Wu, H., Li, Z.-L., 2013. Estimating net surface longwave radiation from net surface shortwave radiation for cloudy skies. Int. J. Remote Sens. 34, 8104–8117.
Zhou, W., Shi, J., Wang, T., Peng, B., Zhao, R., Yu, Y., 2018. Clear-sky Longwave downward radiation estimation by integrating MODIS data and ground-based measurements. IEEE Journal of Selected Topics in Applied Earth Observations and Remote Sensing 1–10.
Zhou, W., Shi, J.C., Wang, T.X., Peng, B., Husi, L., Yu, Y.C., Zhao, R., 2019. New methods for deriving clear-sky surface Longwave downward radiation based on remotely sensed data and ground measurements. Earth and Space Science 6, 2071–2086.
Zhu, Z., Woodcock, C.E., 2012. Object-based cloud and cloud shadow detection in Landsat imagery. Remote Sens. Environ. 118, 83–94.